Parameter-free calculations of X-ray spectra with FEFF9

John J. Rehr,*[a] Joshua J. Kas,[a] Fernando D. Vila,[a] Micah P. Prange[bc] and Kevin Jorissen[a]

Received 15th December 2009, Accepted 27th April 2010
First published as an Advance Article on the web 6th May 2010
DOI: 10.1039/b926434e

We briefly review our implementation of the real-space Green's function (RSGF) approach for calculations of X-ray spectra, focusing on recently developed parameter free models for dominant many-body effects. Although the RSGF approach has been widely used both for near edge (XANES) and extended (EXAFS) ranges, previous implementations relied on semi-phenomenological methods, *e.g.*, the plasmon-pole model for the self-energy, the final-state rule for screened core hole effects, and the correlated Debye model for vibrational damping. Here we describe how these approximations can be replaced by efficient *ab initio* models including a many-pole model of the self-energy, inelastic losses and multiple-electron excitations; a linear response approach for the core hole; and a Lanczos approach for Debye–Waller effects. We also discuss the implementation of these models and software improvements within the FEFF9 code, together with a number of examples.

1. Introduction

Theories of X-ray and electron spectra as well as other "optical constants" have become increasingly sophisticated.[1–4] For example, treatments of such spectra now include a number of key many-body effects such as inelastic losses and vibrational damping. Moreover a number of recent developments go beyond the independent-particle approximation using time-dependent density functional theory (TDDFT) or the Bethe-Salpeter equation (BSE).[5,6] However, current treatments[2,7,8] often utilize simplified or semi-empirical models, with considerable variations in the results. Recently, however, we have made significant progress both in the theory and interpretation of various X-ray spectroscopies. In particular, we have developed parameter free approaches for calculations of the spectra that include the effects of dominant many-body factors. Here we describe the advances, which are applicable to all spectroscopies involving electronic excitation, including among others X-ray absorption spectroscopy (XAS),[2] X-ray Raman scattering (XRS), also known as non-resonant inelastic X-ray scattering (NRIXS),[9] and electron energy-loss spectroscopy (EELS).[10–13]

Our implementation of these developments is based on the real-space Green's function (RSGF) approach[2] within the quasiparticle picture, and differs from all earlier approaches[14–18] in the treatment of several many-body effects. The RSGF approach has been widely applied, especially for extended X-ray absorption fine structure (EXAFS) and X-ray absorption near edge spectra (XANES).[2,19] The terms XANES and EXAFS refer, respectively, to the structure in the X-ray absorption spectrum $\mu(\omega)$ at low and high energies relative to the absorption edge, with the crossover at about 30 eV above threshold. This energy scale is set by typical plasmon excitation energies ω_p, below (above) which inelastic losses due to electronic excitations are relatively weak (strong), leading to strong (weak) scattering. Although EXAFS is now fairly well understood,[2] routine analysis of EXAFS experiments generally makes use of simplified models and several many-body parameters, *e.g.* mean free paths, many-body amplitude factors, and Debye–Waller factors. Similar considerations apply to XANES, where the agreement between theory and experiment is often less satisfactory; in particular our previous approximations *e.g.*, in the FEFF84 code often exhibited excessive loss. Our strategy for improving this approach is as follows: first, the RSGF approach is extended to permit calculations of dielectric response over a broad spectrum including the dominant low-energy region.[20] From the dielectric response, we obtain system dependent self-energies and mean free paths[21,22] as well as intrinsic losses due to multi-electron excitations using GW and related methods.[23] Second, from auxiliary first principles calculations of the dynamical matrix and an efficient Lanczos algorithm, we obtain vibrational damping in terms of multiple-scattering Debye–Waller factors. Together with advances in analysis, algorithms, and computer power, these developments yield improved calculations of both EXAFS and XANES as well as optical constants and X-ray scattering factors over a broad spectrum from the UV to X-ray energies for large complex systems.[24] This strategy has been implemented within the FEFF9 code which is a major improvement over FEFF8.4. In addition, the FEFF9 code has other new capabilities and features compared to previous versions of FEFF, including several new spectroscopies. The code also has improved memory management and a new graphical user interface (GUI). In addition there is an option to run FEFF9 in a virtual cloud computing environment.[25]

[a] *Department of Physics, University of Washington, Seattle, WA 98195, USA*
[b] *Department of Physics and Astronomy, Vanderbilt University, Nashville, TN 37235*
[c] *Materials Science and Technology Division, Oak Ridge National Laboratory, Oak Ridge, TN 37831, USA*

The organization of this article is as follows: In the next section we briefly describe the quasi-particle theory of XAS within the multiple-scattering (MS) real-space Green's function formalism. We then discuss our recent theoretical developments, which include (1) full spectrum optical constants; (2) inelastic losses and multi-electron excitations; (3) treatment of the core hole; (4) *ab initio* Debye–Waller factors; and (5) combined real and k-space methods. Subsequently, we give an overview of new applications to EELS and NRIXS. We then summarize new features available to FEFF9 users, including a graphical user interface (GUI), improved memory management, and a novel use of scientific "cloud computing." Finally, we illustrate the theory with a number of examples together with some concluding remarks.

2. Quasi-particle theory of XAS

The basic independent-particle theory of XAS is now well developed,[2,14–18] but the theory ignores many important many-body effects. Thus current theoretical efforts are directed towards first principles calculation and modeling of many-body effects beyond the independent particle approximation. In this section we give a brief introduction to the quasi-particle theory of XAS as implemented in our RSGF approach, which addresses some of these limitations.

Schematically an X-ray absorption experiment measures the X-ray absorption coefficient $\mu(\omega)$, which characterizes the decay in intensity I of an X-ray beam passing through a material of thickness d, *i.e.*, $I(d) = I_0 e^{-\mu(\omega)d}$. The contribution to $\mu(\omega)$ at X-ray energy $\hbar\omega$ is proportional to the total absorption cross-section $\sigma(\omega)$. For a given material this cross-section can be calculated in terms of the many-body ground $|0\rangle$ and excited N-particle states $|F\rangle$ of the system using Fermi's golden rule,

$$\sigma(\omega) = 4\pi^2 \frac{\omega}{c} \sum_F |\langle 0|d|F\rangle|^2 \delta(\omega + E_0 - E_F). \qquad (1)$$

Here d represents the coupling to the X-ray field, E_0 the ground-state energy, E_F the excited-state energies, and we have used atomic units ($e = \hbar = m = 1$).

Many current calculations are based on the reduction of the many-body golden rule in eqn (1) to an independent-electron approximation with a dipole approximation $d = \hat{\varepsilon}\cdot\boldsymbol{r}$ for the interaction. The sum over excited states F then becomes a double-sum over "initial" (occupied) independent-electron states $|i\rangle$ and "final" (unoccupied) one-particle states $|f\rangle$. In this simple physical picture, the absorbed photon kicks a core-electron of energy E_i into a (photoelectron) state above the Fermi-level of energy $E \equiv E_i + \omega$.

The differences among the various theoretical approaches reflect different approximations for the calculation of these ingredients. In particular, the question of which independent-electron states to use is ambiguous and depends on the energy range of interest. Ideally the independent-electron Hamiltonian should contain all of the many-body effects, including the interaction with the core hole, as well as core hole and photoelectron lifetime effects. However, approximations of these effects are essential for any practical calculation. Commonly used approaches are based on the "final state rule" (FSR) for the core hole interaction, and the use of an appropriate quasi-particle self-energy model for the treatment of photo-electron lifetime effects. Theoretical justifications for these approximations have recently been developed and also establish a close connection between the final state rule and BSE calculations for deep-core spectra within an effective one-particle Green's function theory.[23,26]

2.1 Real-space Green's function formalism

An explicit calculation of the final states in the independent-electron golden rule is often a computational bottleneck at high energies and can only be carried out efficiently for systems which are small or periodic. Even for periodic solids many single-particle approximations (including the final state rule) destroy periodicity due to the presence of a core hole. In addition inelastic losses are difficult to account for within wave function based methods. Fortunately, explicit calculations of the final states can be avoided by re-expressing the XAS in terms of the retarded RSGF of the photoelectron and its spectral representation

$$G(E) = \frac{1}{E - h' + i\Gamma} = \sum_f |f\rangle \frac{1}{E - E_f + i\Gamma} \langle f|. \qquad (2)$$

Here $h' = p^2/2 + V'_{\mathrm{Coul}} + \Sigma(E)$ is the final state Hamiltonian, V'_{Coul} is the Coulomb potential which includes a screened core hole, $\Sigma(E)$ is an energy-dependent self-energy, and Γ is the core hole lifetime, and $|f\rangle$ denotes the quasi-particle eigenstates of h'. A detailed justification of the RSGF approach is provided by the quasi-boson approach,[23] where the Green's function in eqn (2) is an effective propagator in the presence of a core hole, and multi-electron effects (see below) are treated in terms of a spectral function.

In practice we have found that a self-consistently screened core hole[2] gives a core hole potential similar to that from linear response,[6] as in the BSE. Clearly, the spectral representation of the Green's function, as given by the right hand term in eqn (2), implicitly sums over final states. This significantly reduces the computational effort by eliminating the need for explicit calculations of the final state eigenfunctions. Thus the RSGF formalism greatly simplifies calculations of XAS, especially for complex, aperiodic systems. The approach also gives rise to a physical picture of the scattering processes in real-space in terms of a MS path expansion. In practice the RSGF method can only accommodate a finite cluster of atoms. However, this does not pose a limitation to the calculation of XAS, since inelastic losses limit the range probed by XAS experiment to a region comparable to the mean free path λ. Since λ is typically between 5–20 Å for XAS, this corresponds to clusters of order 10^2 atoms about a given absorption site. This also explains why the quasi-particle theory of XAS is intrinsically a *short range order* theory.

The RSGF formalism naturally separates into intra-atomic contributions from the central (absorbing) atom G^c and MS contributions from the environment G^{sc}. Thus $G = G^c + G^{sc}$, so that the XAS can be factored as $\mu = \mu_0(1 + \chi)$. As a result, the structure in μ depends to leading order on the "embedded" atomic background μ_0 (*i.e.*, that defined by the solid-state potential at the absorption site) and on the *fine structure* χ due

to MS from the environment. Within the RSGF approach it is generally convenient to represent G in an angular momentum $L = (\ell,m)$ basis about each atomic site in the sample. This yields the expression for the contribution to the XAS from a given core initial state $|i\rangle$ at site R,

$$\sigma(E) = 4\pi^2 \frac{\omega}{c} \sum_{L,L'} M^*_{L,i}(E)\rho_{L,L'}(E)M_{L',i}(E). \qquad (3)$$

Here $M_{L,i}$ is the dipole matrix element between the core state and a scattering state $|L\rangle$ of angular momentum L, $\rho_{L,L'}(E) = -(1/\pi)\mathrm{Im}[G_{L,L'}(E)]$ is an element of the spectral density matrix at the absorbing atom, and for simplicity the site indices R and R' are suppressed. The scattering part of G may be expressed as a sum over all MS paths that a photoelectron can take away from the absorbing atom and back: first the photoelectron can scatter at any site in the sample, and second the scattering within an individual site R can be summed using a "site t-matrix". This yields a MS *path expansion* of the scattering contribution to the propagator

$$G^{sc}_{L,L'} = [\bar{G}^0 T \bar{G}^0 + \bar{G}^0 T \bar{G}^0 T \bar{G}^0 + \cdots]_{L,L'}, \qquad (4)$$

where the successive terms represent single, double, and higher order scattering processes. Typically, the maximum value of ℓ necessary for accurate EXAFS calculations using eqn (4) is $\ell_{\max} = 25$ or less for excitations up to about $E = 1000$ eV above threshold.[27] The T matrix has elements $T_{LR,L'R'} = t_{\ell R}\delta_{R,R'}\delta_{L,L'}$, where t includes all repeated scatterings within a given atomic cell. It is important to point out that in the above expression $\bar{G}^0$ refers to the damped free Green's function as calculated with a complex self-energy and core hole lifetime, and subject to the condition that the site diagonal matrix elements $\bar{G}^0_{LR,L'R}$ are set to zero.

At high energies the MS path expansion turns out to converge rapidly, typically with only of order 10^2 paths. This fast convergence is due to weakness of scattering (*i.e.*, the elements of T are small), and damping arising from the inelastic mean free path in the EXAFS energy regime (*i.e.*, the elements of G^0 for large $|R - R'|$ are small). Moreover, the MS expansion sometimes converges adequately in XANES, particularly for deep core hole absorption in heavy elements which have short core hole lifetimes. However, when the convergence is poor, the MS expansion must be carried to very high or all orders (full MS or FMS), *e.g.*, by explicit matrix inversion[28] or Lanczos matrix inversion algorithms,[29] *i.e.*,

$$G^{sc}_{L,L'} = [(1 - \bar{G}^0 T)^{-1}\bar{G}^0]_{L,L'}. \qquad (5)$$

The dimension of the matrix to be inverted in solving eqn (5) is $N(\ell_{\max} + 1)^2$, where N is the number of atoms in the cluster and $\ell_{\max}$ is the maximum allowed angular momentum. For example, in a cluster of size 500 atoms in order to limit the matrix size to less than $10^4 \times 10^4$ one must limit the maximum ℓ value to 3 or less. Thus, since the maximum ℓ necessary for accurate calculations increases with energy relative to the edge, the FMS inversion is useful only for XANES calculations. The relativistic generalization of eqn (5) is similar in form, the key formal difference being that the angular momenta are replaced with their relativistic generalization[30–32] $L = (\kappa, m)$. Relativity is important for the treatment of spin–orbit coupling, which is large in the atomic core states and hence in transition matrix elements for large Z atoms. On the other hand, relativity has only weak effects on the scattering and propagation of the photoelectron. In the FEFF multiple scattering codes, these effects are treated to high accuracy using a relativistic Dirac-Fock approach[33] for atomic states and a semi-relativistic approximation for propagation.

The calculation of the scattering potentials to construct the site t-matrices simplifies for electrons at moderate energy (*i.e.* several eV above threshold), where the scattering depends strongly only on the potential in the core of an atom. In this deep core region, spherical symmetry of the potential is a good approximation. Self-consistent field (SCF) calculations of the potentials are nevertheless desirable even for EXAFS, since the Fermi energy threshold must be known to an accuracy better than a few eV for distance determinations better than 0.01 Å. In the SCF procedure in FEFF8 and FEFF9, Coulomb potentials, electron densities, and the Fermi energy are iterated typically 10–20 times. As a result of hybridization and chemical bonding, the self-consistent atomic electron configurations in solids usually differ from those in isolated atoms, and in general yield *fractional* average occupations of the various atomic levels. Comparisons with full-potential ground state electronic structure codes have shown that the spherical approximation is often valid for XAS, except within a few eV of threshold. However, muffin-tin corrections can be important near threshold, especially in small anisotropic systems. Thus, the development of efficient, full-potential RSGF approaches beyond the spherical muffin-tin approximation remains an important challenge for more accurate XANES calculations.[34–36] Such full-potential calculations are now standard in a number of XANES codes, *e.g.*, plane-wave pseudopotential codes like PARATEC[3,37] and the finite-difference approach in FDMNES.[38] However, the implementation of full-potential corrections in FEFF9 is still developmental.[34]

2.2 Path expansion and the EXAFS equation

Due to the large dimension of G, exact calculations with the path expansion can be carried out efficiently only for a few low-order MS paths.[39] To overcome this computational bottleneck, an efficient method based on the Rehr-Albers (RA) scattering matrix formalism[40] has been devised. The RA approach yields curved-wave calculations of the effective scattering amplitude $f_{\mathrm{eff}}(k)$ (from which the FEFF code takes its name) in terms of a separable representation of the free propagator $G^0(E)$. With this representation the MS expansion can be re-expressed as a sum over MS paths R in a form similar to the original EXAFS equation of Sayers, Stern and Lytle,[41]

$$\chi(k) = S_0^2 \sum_R \frac{|f_{\mathrm{eff}}(k)|}{kR^2}\sin(2kR + \Phi_k)e^{-2R/\lambda_k}e^{-2\sigma^2k^2}. \qquad (6)$$

An important difference, however, is the overall many-body amplitude factor S_0^2, reflecting the lack of orthogonality between initial and final states with and without the core hole. Here $k = [2(E - E_F)]^{1/2}$ is the wavenumber measured from

threshold E_F, and $\lambda_k \approx k/(|\mathrm{Im}\ \Sigma| + \Gamma/2)$ is the XAFS mean free path, which is calculated in terms of the self-energy and core hole lifetime Γ. Finally σ, which characterizes the thermal and structural disorder, is the rms fluctuation in the *effective path length* $R = R_{\mathrm{path}}/2$, which corresponds to peaks in the EXAFS Fourier transform. This equation has been automated in the FEFF codes and is now widely used to analyze EXAFS data. In addition, eqn (6) illustrates the dominant many-body "inelastic parameters" S_0^2, λ_k and the vibrational DW factors σ^2, which we now show can be calculated from first principles.

3. Recent developments in FEFF

In this section we discuss our recent developments in the treatment of the key many-body effects on deep core excitation spectra with the FEFF codes. From a many-pole representation of the dielectric function and the GW approximation, we obtain photoelectron self-energies, inelastic mean free paths (IMFPs), and contributions from multi-electron excitations. Next, core hole screening is treated *via* a random phase approximation (RPA) calculation of the local response function, which is then used to calculate the screened core hole interaction. Finally, from calculations of the dynamical matrix and a many-pole Lanczos algorithm, we obtain phonon spectra and Debye–Waller (DW) factors. By iterating these steps, we then obtain calculations of optical constants from the UV to X-ray energies. All of the above procedures have been introduced into calculations of excited state spectra based on the real-space Green's function formalism described in the previous section.[2]

3.1 Full-spectrum calculation of optical constants

A key physical quantity in these calculations is the dielectric response function $\chi(\omega)$.[1] In the long wave-length limit, various optical constants are related to $\chi(\omega)$ through the local atomic polarizability $\alpha(\omega)$,[42]

$$\alpha(\omega) \equiv \int \mathrm{d}\boldsymbol{r}\mathrm{d}\boldsymbol{r}'\ d^{\dagger}(\boldsymbol{r})\chi(\boldsymbol{r}, \boldsymbol{r}', \omega)d(\boldsymbol{r}), \tag{7}$$

where the $d(\boldsymbol{r})$ represents the dipole coupling to the photon field and; for simplicity, we ignore weak non-dipole interactions. Our RSGF approach for calculating $\alpha(\omega)$ is described by Prange *et al.*[20] and Ankudinov *et al.*[6] and summarized below. Here we describe only the methods used to obtain the response function $\chi(\boldsymbol{r}, \boldsymbol{r}'; \omega)$ within the RSGF formalism. The ingredients used are discussed in the following sections.

We split the response function into two contributions. One contribution is due to transitions from the valence band to the conduction band, *i.e.* valence response, while the other is due to transitions from localized atomic-like core states, that is, core response.

To obtain the core response, we calculate $\mathrm{Im}[\alpha(\omega)] = \Sigma_{i,L,L'} \tilde{M}_{i,L} \langle \rho_{L,L'}(E) \rangle \tilde{M}_{L'i}$ by summing the contributions from all occupied core states i.[20] Here, $\tilde{M}_{i,L}$ are screened dipole matrix elements between occupied core states $|i\rangle$ and final scattering states $|L, 0\rangle$, and $\rho_{L,L'}(E)$ are matrix elements of the spectral density operator $\rho(E) = (-1/\pi)\mathrm{Im}[G(E)]$ in an angular momentum and site basis.[6] The brackets $\langle \cdots \rangle$ denote a configurational average, which is expressed in terms of DW factors. For each core state $|i\rangle$, we first calculate the atomic-like background with no scattering; fine structure is then added with full multiple scattering to about 50 eV, and then with the MS path expansion to about 1500 eV above each edge.

In order to sum over all transitions from the valence band, we express the bare response in terms of Green's functions alone, without reference to either occupied or unoccupied Kohn–Sham orbitals, *i.e.*,

$$-\frac{1}{\pi}\mathrm{Im}[\chi^0(\boldsymbol{r}, \boldsymbol{r}'; \omega)] = \int_{E_F-\omega}^{E_F} \mathrm{d}E \rho(\boldsymbol{r}, \boldsymbol{r}'; E)\rho(\boldsymbol{r}, \boldsymbol{r}'; E + \omega). \tag{8}$$

Here $\rho(\boldsymbol{r}, \boldsymbol{r}'; E)$ is the imaginary part of the Green's function and E_F is the Fermi energy. The dielectric response $\varepsilon_2(\omega)$ is then given by

$$\varepsilon_2(\omega) = \frac{4\pi}{V}\mathrm{Im} \int \mathrm{d}r\mathrm{d}r'\ \mathrm{Tr}[d\chi(\boldsymbol{r}, \boldsymbol{r}'; \omega)d^{\dagger}], \tag{9}$$

where V is the full system volume and d is the dipole interaction.

The full response function $\chi(\boldsymbol{r}, \boldsymbol{r}'; \omega)$ is related to the bare response by

$$\chi = \chi^0\ (1 - \boldsymbol{K}\chi^0)^{-1} \tag{10}$$

where $\boldsymbol{K}$ is the particle-hole interaction kernel which incorporates local field effects. Because the expression of the bare response involves an integral over all space, the Green's function $G(\boldsymbol{r}, \boldsymbol{r}'; \omega)$ for all $\boldsymbol{r}$ and $\boldsymbol{r}'$ is required. This is a fundamental difference from calculations of core response, where the arguments of the Green's function are limited by the finite extent of the core excited state. Thus the multiple scattering formalism given in section 2.1 must be modified. For more complete details we refer the reader to Prange *et al.*[20] However, this development is not yet integrated into FEFF9.

From the above results, we can obtain the imaginary part of the bulk dielectric response $\varepsilon_2(\omega)$ at all frequencies. The real part $\varepsilon_1(\omega)$ is then obtained from a Kramers transform. From the complex dielectric function, we can calculate a variety of other optical constants, including the complex index of refraction, the absorption coefficient, and the loss function $\mathrm{L}(\omega) = -\mathrm{Im}[\varepsilon^{-1}(\omega)]$, which is an important ingredient for our calculations of inelastic losses.

3.2 Many-pole model of inelastic losses

From the dielectric response, we can obtain the self-energy $\Sigma(E)$ *via* the "GW approximation" of Hedin and Lundqvist[43]

$$\Sigma(E) = i \int \frac{\mathrm{d}\omega}{2\pi} G(E - \omega) W(\omega) e^{-i\delta\omega}, \tag{11}$$

where $W = \varepsilon^{-1}(\omega)V$ is the screened coulomb interaction. For the sake of efficiency, we use a free Green's function in these calculations, which produces an *average* self-energy. We then represent the dielectric function $\varepsilon(\boldsymbol{q},\omega)$ with a sum of poles,

$$-\mathrm{Im}[\varepsilon^{-1}(\boldsymbol{q}, \omega)] = \frac{\pi}{2}\sum_j g_j \omega_j\, \delta(\omega - \omega_j(\boldsymbol{q})), \tag{12}$$

where $g_j = (2\Delta\omega_j/\pi\omega_j)\ \mathrm{Im}\ [\varepsilon^{-1}(\omega_j)]$ is the strength of pole j, and $\Delta\omega_j$ is the pole spacing. For simplicity, the momentum dependence of each pole is approximated by a polynomial

in q^2: $\omega_j(\boldsymbol{q}) = [\omega_j^2 + v_F^2 q^2/3 + q^4/4]^{1/2}$.[44] This approximation is roughly consistent with explicit calculations[9] and has the correct high q limit. The precise dispersion is not crucial, since $\boldsymbol{q}$ and ω are integrated over.[44] This model is matched to our *ab initio* loss function $L(\omega) = -\mathrm{Im}[\varepsilon^{-1}(\omega)]$ at zero momentum transfer. This gives a sum of single-pole self-energy models $\Sigma_1(E;\omega_j)$ with excitation energies ω_j, *i.e.*, $\Sigma(E) = \sum_j g_j \Sigma_1(E,\omega_j)$.

Many-pole models[45] and other methods[46] have been developed previously for more accurate self-energy calculations; however, they are computationally demanding and not applicable at high photoelectron energies, *e.g.*, for EXAFS. Our model is similar to that of von der Linden and Horsch[7] but does not rely on empirical optical constants. Our algorithm for the many-pole dielectric function of eqn (12) is key to an efficient calculation of the many-body effects in core-level XAS,[22] and should be widely applicable. Figures 4, 6 and 7 show the effects of inelastic losses on the near edge spectra of a variety of materials.

We can also calculate the IMFP $\lambda = (E/2)^{1/2}/|\mathrm{Im}\,\Sigma(E)|$ for various materials.[47] Figure 1 shows λ for fcc Cu using a 100-pole model. Clearly this model corrects the excessive loss of the single-pole model below 100 eV, and yields good agreement with fits to experiment.[48] Our self-energy is also in reasonable agreement with that of Soininen *et al.*[45] Similar approaches[21] can be applied to calculations of stopping powers in inelastic electron scattering[49] and photoemission spectra.[8]

3.3 Multi-electron excitations

Our many-pole self-energy (MPSE) model in eqn (12) also yields estimates of inelastic losses due to multi-electron (*e.g.* "shake-up" and "shake-off") excitations. These can be calculated with a generalization of the GW approximation using the quasi-boson model, as described in detail in Campbell *et al.*[23] Such excitations correspond to satellites beyond the quasi-particle peak in the spectral function $A = (-1/\pi)\mathrm{Im}G_{\mathrm{eff}}$, where G_{eff} is an effective one-particle propagator. In addition to intrinsic losses, G_{eff} contains energy-dependent interference terms which tend to suppress the satellites. The net effect can

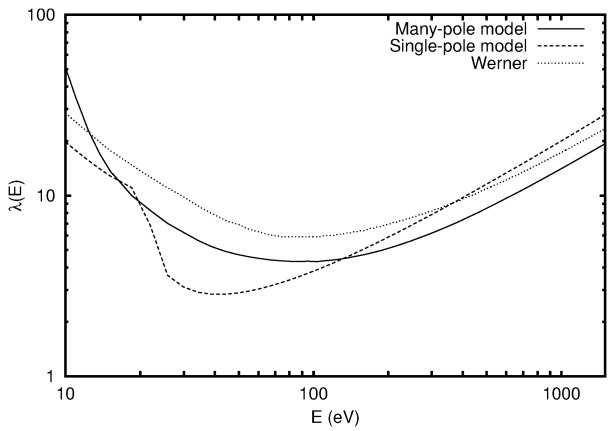

Fig. 1 Inelastic mean free path λ for fcc Cu for our many-pole model (solid), a single plasmon-pole model (dashes); and a fit to experiment (dots).[48]

be included in the X-ray absorption $\mu(\omega)$ in terms of a convolution of a normalized spectral function $\tilde{A}$ and the quasi-particle absorption coefficient μ_{qp}, which ignores satellites,

$$\mu(\omega) = \int_0^\infty d\omega' \tilde{A}(\omega,\omega')\mu_{qp}(\omega-\omega') \equiv \langle \mu_{qp}(\omega) \rangle, \qquad (13)$$

where ω' is the excitation energy.[23] Likewise, the EXAFS including multi-electron excitations is given by a convolution of $\tilde{A}$ with the quasi-particle fine structure. For each MS path R, the convolution over the fine structure yields an amplitude reduction factor $S_R^2(\omega)$ and (since $\tilde{A}$ is asymmetric) a negative phase shift $\Delta_R(\omega)$, $\langle e^{2ikR} \rangle = S_R^2(\omega) e^{2ikR + \Delta_R(\omega)}$. For example, for the first shell of Cu, we find that $S_R^2(\omega)$ and $\Delta_R(\omega)$ cross-over smoothly from the adiabatic (or quasi-particle) limit at threshold to nearly constant values $S_0^2 \approx 0.92$ and $\Delta_R \approx -0.2$ rad in the EXAFS. This behavior is roughly consistent with experiment (see Fig. 5) where $S_R^2 \approx 0.9$.[23]

Nevertheless, the implementation of the RSGF theory in FEFF9 currently neglects atomic multiplet effects. Including such effects requires a multi-configurational treatment of local atomic-excitations or an extension of the quasi-boson approach.[23] Presently such multiplet effects are usually treated using crystal-field corrections to atomic calculations.[50] Although there have been significant recent developments,[51] adding multiplet effects to *ab initio* calculations remains an important challenge.

3.4 Improved core hole interaction

Several methods have been used to improve upon the FSR approximation for the core hole interaction. One is based on the BSE formalism, which goes beyond the single particle picture by explicitly considering particle-hole wave functions. The other is TDDFT, which is an extension of the standard Kohn–Sham density functional theory to treat excited states. Methods based on BSE tend to be time consuming because one must calculate a four-point response function $\chi(r_1,r_2,r_3,r_4)$. TDDFT methods, while less time-consuming, incorporate a local exchange–correlation functional f_{xc} which can be inadequate to describe excitonic states. Thus we have combined these techniques in an effort to overcome these difficulties. Both the BSE and TDDFT methods depend on the calculation of the response function in eqn (10). In our combined approach we separate the kernel $\boldsymbol{K}$ into local and nonlocal terms $\boldsymbol{K} = \boldsymbol{K}_{\mathrm{L}} + \boldsymbol{K}_{\mathrm{N}}$, where

$$\begin{aligned} \boldsymbol{K}_{\mathrm{L}}(\boldsymbol{r},\boldsymbol{r}';\omega) &= v(\boldsymbol{r},\boldsymbol{r}') + f_{xc}(\boldsymbol{r},\boldsymbol{r}';\omega) \\ \boldsymbol{K}_{\mathrm{N}}(\boldsymbol{r},\boldsymbol{r}';\omega) &= W(\boldsymbol{r},\boldsymbol{r}') - f_{xc}(\boldsymbol{r},\boldsymbol{r}';\omega). \end{aligned} \qquad (14)$$

Here $v(\boldsymbol{r},\boldsymbol{r}')$ is the Coulomb interaction, $W(\boldsymbol{r},\boldsymbol{r}') = \varepsilon^{-1}v(\boldsymbol{r},\boldsymbol{r}')$ is the screened Coulomb interaction, and ε is the dielectric function. We calculate $W(\boldsymbol{r},\boldsymbol{r}')$ within the random phase approximation (RPA), following Zangwill and Soven,[42] while the response functions are calculated using the projection-operator method of Nesvizhskii *et al.*[52] which treats the core hole screening at the atomic level and is very efficient. See Ankudinov *et al.*[6] for additional details.

3.5 Debye–Waller factors

As noted above, the analysis of XAS spectra requires the knowledge of Debye–Waller factors arising from thermal vibrations and structural disorder. These factors can be important in XANES and are an essential component of the EXAFS equation, *i.e.*, eqn (6). They result from the thermal and configurational average $\langle\mu(E)\rangle$ of the X-ray absorption coefficient $\mu(E)$ over the pair (or MS path length) distribution function. The vibrational and structural disorder effects are additive. Structural disorder dominates in the near-edge region, and depends on external factors like sample history and preparation. Currently, this kind of disorder can be included in FEFF9 by means of configurational averaging using, for instance, structures sampled from molecular dynamics simulations.[53] In this section we will focus only on the vibrational contribution, which is crucial in quantitative EXAFS analysis.

The DW factors vary as $\exp[-W(T)]$ where $W(T) \approx 2k^2\sigma^2(T)$, and $\sigma^2(T) = \langle[\boldsymbol{u}_R - \boldsymbol{u}_0)\cdot\hat{\boldsymbol{R}}]^2\rangle$ is the mean square relative displacement (MSRD) of a given MS path.[54] This causes damping of the spectra with respect to increasing temperature T and wave number k. The thermal effects on the normalized EXAFS spectrum $\chi(k)$ are dominated by the average over the oscillatory behavior $\langle\chi_R(k)\rangle \propto \langle\sin(2kR + \Phi)\rangle$ of each path of length R in the MS path expansion. These thermal averages are given by Debye integrals over the vibrational density of states (VDOS) $\rho_R(\omega)$ projected onto a given MS path R:[55–57]

$$\sigma_R^2(T) = \frac{\hbar}{2\mu_R}\int_0^\infty \frac{1}{\omega}\coth\left(\frac{\beta\hbar\omega}{2}\right)\rho_R(\omega)\,\mathrm{d}\omega. \qquad (15)$$

Here μ_R is the reduced mass associated with the path R, and $\beta = 1/k_\mathrm{B}T$.

In previous FEFF versions, the DW factors have been estimated mostly by means of a semi-empirical Einstein or Debye model VDOS,[58,59] or fitted to experimental data. Although those approximations are quite useful, they are not completely satisfactory for several reasons: (1) the available experimental data only allow reliable fits to a few parameters; (2) semi-empirical models require different Debye or Einstein temperatures for different MS paths; and (3) such models do not capture the anisotropic structure of the phonon spectra.[55,60] In FEFF9 these limitations are largely avoided by calculating the VDOS using a continued fraction representation of the lattice dynamical Green's function (LDGF) generated with the iterative Lanczos algorithm.[61] From the imaginary part of the LDGF we have[55,56]

$$\rho_R(\omega) = -\frac{2\omega}{\pi}\mathrm{Im}\left\langle Q_R\left|\frac{1}{\omega^2 - \boldsymbol{D} + i\varepsilon}\right|Q_R\right\rangle, \qquad (16)$$

where $|Q_R\rangle$ is a Lanczos seed state representing a normalized, mass-weighted displacement of the atoms along the path R, and $\boldsymbol{D}$ is the dynamical matrix of force constants

$$D_{jl\alpha,j'l'\beta} = (M_j M_{j'})^{-1/2}\frac{\partial^2 E}{\partial u_{jl\alpha}\partial u_{j'l'\beta}}, \qquad (17)$$

where $u_{jl\alpha}$ is the $\alpha = \{x,y,z\}$ Cartesian displacement from the equilibrium position of atom j in unit cell l, M_j is the mass of atom j, and E is the total internal energy of the system. Within this formulation, the problem is reduced to finding an accurate model for $\boldsymbol{D}$. Empirical estimates of the interatomic force constants are sometimes available, but their temperature dependence limits their accuracy and generality. Alternatively, first principles electronic structure methods can now be used to determine $\boldsymbol{D}$ with sufficient accuracy for both periodic and molecular systems.[62–64] For crystalline systems $\boldsymbol{D}$ can be obtained *e.g.*, using the ABINIT[65] and Quantum Espresso[66] codes. For molecular systems, the force constant matrix $\boldsymbol{D}$ (*i.e.* the Hessian) can be obtained with Gaussian 03.[67]

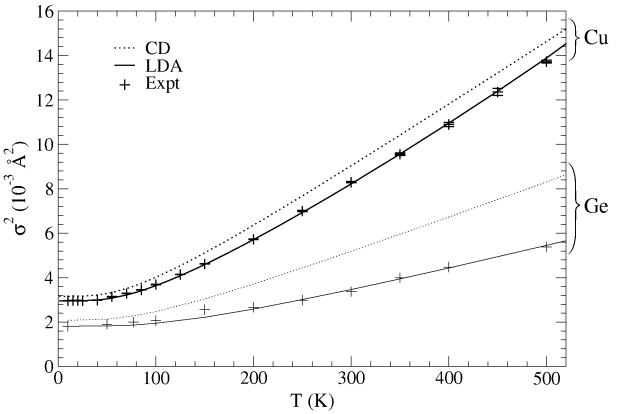

Fig. 2 Temperature dependence of the Debye–Waller factor for the nearest neighbor single scattering path in Cu and Ge. The experimental difference values (from Fornasini *et al.*[68] for Cu and Dalba *et al.*[69] for Ge) were shifted to match the LDA results at 0 K.

Figure 2 shows typical results for Cu and Ge, obtained with the local density approximation (LDA)[70,71] and, for comparison, the correlated Debye (CD) model. Note that the LDA results are in good agreement with experiment.[68,69] While the CD model[2] works well for fcc Cu, the model gives significant errors for the more anisotropic diamond structure in Ge.

The Lanczos method to calculate the EXAFS DW factors depends only on the path-length distribution function. Therefore, it also applies to related spectroscopies which can be described by a MS path expansion. For instance, the EXAFS DW factors are analogous to those arising in X-ray and neutron diffraction, in which case $W(T) = (1/2)k^2u^2(T)$, and $u^2(T) = \langle(\boldsymbol{u}\cdot\boldsymbol{r})^2\rangle$ is the mean-square atomic displacement. These related factors can also be calculated within FEFF9 using an appropriate seed displacement $|Q_R\rangle$ to obtain corresponding projections of the VDOS.[71] For instance, a displacement involving a single atom produces u^2, while a displacement orthogonal to a path vector yields $\sigma_\perp^2$. Finally, the main effects of anharmonicity can be included by calculating the dynamical matrix for equilibrium positions corresponding to a temperature-dependent lattice constant $a(T)$.[71] This method yields the net thermal expansion $\Delta a = a(T) - a_0$. Also, including the perpendicular component of the expansion $\sigma_\perp^{(1)} = \langle|\Delta\boldsymbol{u}_\perp|^2\rangle/(2R_0)$, yields the first EXAFS cumulant. For example, the first cumulant of Cu at 300 K is 0.0217 Å in good agreement with the experimental value 0.0205 ± 0.0009 Å.[68] Estimates for the third cumulant can be obtained using cumulant relations.[71]

3.6 Combined real and *k*-space calculations

For some systems, real-space calculations can be time consuming, especially for energies at which the photoelectron has a long mean free path. These situations require that a very large cluster of atoms be used for calculations, which translates to the inversion of a very large FMS matrix. Thus it is advantageous to use a *k*-space method for these systems. However, as mentioned earlier in this article, core hole effects are difficult to treat within *k*-space methods and require large supercells to reach convergence. We have implemented a scheme in which the crystal is treated in *k*-space, *i.e.* *via* the Korringa-Kohn-Rostoker (KKR) Green's function method,[72–74] and the core hole is treated subsequently in real-space.[12] Briefly, we calculate the KKR Green's function for the ground state of the system without a core hole. The ingredients needed to perform this calculation are the same as those of the MS RSGF method, *i.e.* the single site scattering matrices $t_{\ell R}$, and the structure factor, which is the Fourier transform of the free propagator $G^0_{RLR'L'}$ in site and angular momentum basis. Once the KKR Green's function is found, we transform back to the site basis to obtain the full Green's function $G_{RLR'L'}$ of the ground state system. The final state Green's function (including the core hole) can then be obtained from the central atom scattering matrices with and without a core hole:

$$G_{\mathrm{FS}} = G_{\mathrm{GS}}[1-\Delta t G_{\mathrm{GS}}]^{-1}, \quad (18)$$

where $\Delta t = t_{FS} - t_{GS}$ is the difference between the final state and ground state scattering matrices. An example of this approach for GaN is presented in section 5.

3.7 Other spectroscopies

FEFF9 also has the capability to produce a wide variety of spectral results in addition to those available with FEFF8, including NRIXS, relativistic EELS, X-ray emission spectra (XES) and dichroic spectra, *e.g.*, X-ray linear dichroism (XLS) and magnetic circular dichroism (XMCD). Because theories of electronic excited state spectra are based on Fermi's golden rule expressions similar to eqn (1), the real-space multiple scattering framework in FEFF can be easily adapted to a variety of spectroscopic calculations. For example, XES is theoretically similar to XAS but involves transitions between the core level and occupied valence states, rather than to the unoccupied states. Also, both non-relativistic EELS[11–13,75] and NRIXS[9] spectra can be expressed (up to a prefactor) in terms of similar golden rule expressions, except that instead of the dipole operator in the expressions for XAS and XES the transition operator d is replaced by

$$d = e^{i\boldsymbol{q}\cdot\boldsymbol{r}}. \quad (19)$$

Here $\boldsymbol{q}$ is the momentum transfer, and ω represents the energy loss instead of the photon energy. When q is small, the matrix elements reduce to the dipole operator, and both the EELS and NRIXS spectra become very similar to XAS. However, if q is not small, the dipole selection rules do not apply. One can then obtain information about the excited state density of states (DOS) which is not available from XAS. This fact has been used to extract the excited state DOS directly from experimental NRIXS.[9,76] For the relativistic generalization of EELS, the transition operator d becomes anisotropic and an additional relativistic prefactor is needed.[13] This generalization is also implemented in FEFF9. Examples of our relativistic calculations for the EELS of GaN and for the XES of NH_4NO_3 are shown in Fig. 8 and 9.

4. Software improvements in FEFF9

In addition to improved theoretical methods, FEFF9 has a number of features which make it even more user friendly compared to previous versions. The most notable of these are: (1) a new GUI, (2) improved memory management, and (3) the ability to run within a cloud compute cluster. The code is now accessible to a wide variety of users, from beginners to experts, within a number of operating systems. Our GUI, named JFEFF (JAVA FEFF), is self-explanatory and easy to use. Notable features include a plotting window to show the results and a molecular structure viewer based on Jmol. Figure 3 shows a screenshot of JFEFF with the plotting and structure viewing windows open. The GUI is written in Java and runs on most operating systems, including Windows, MacOS and Linux.

In addition, the FEFF9 code has been reformatted to conform to the Fortran 95 standard. This standard allows for improved memory management compared to Fortran 77, which was used in all previous versions of FEFF. In particular, it is no longer necessary to recompile the code in order to increase the cluster size or alter the angular momentum cutoff.

Cloud computing refers to the large, virtualized pools of compute resources like those offered by Amazon Web Services,[77] and provides a new and possibly advantageous compute paradigm for scientific research. We have recently demonstrated the feasibility of scientific computation using these cloud computing resources, as an alternative to traditional tools.[25] For example, we have shown that cloud computing can provide convenient access to reliable, high-performance clusters, without the need to purchase and maintain sophisticated hardware. We have also developed a set of tools which makes Amazon's Elastic Compute Cloud[78] (EC2) behave like a virtual homogeneous computer cluster. They consist of a set of Bash scripts that perform the basic tasks involved in efficiently interacting with a virtual cluster, including: launching, connecting to, transferring files to and

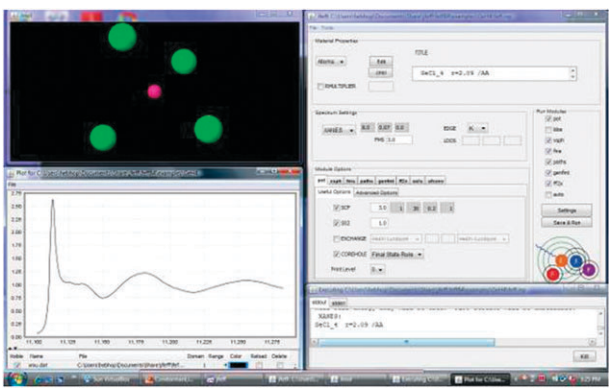

Fig. 3 JFEFF screenshot showing the main window, plotting window, and structure viewer.

from, monitoring, and terminating such clusters. These tools work in conjunction with an EC2 virtual computer environment or Amazon Machine Image (AMI) especially configured for FEFF users. The FEFF AMI includes JFEFF, precompiled versions of FEFF and all the necessary software to run it efficiently in both serial and parallel mode. Using this setup we found that the virtual EC2 environment provides serial and parallel FEFF performances comparable to those obtained on a conventional physical computer cluster.

5. Results

Calculations based on extensions of the quasi-particle theory and the RSGF formalism now make possible a general treatment of XAS, encompassing XANES and EXAFS, as well as a number of other X-ray spectroscopies. Heretofore these calculations have relied on simplified models to deal with many-body effects. However, recent theoretical advances have led to efficient, *ab initio* approaches for calculations of the key many-body damping factors in these core-level X-ray spectroscopies without the need for semi-empirical parameters. Our results show that the new approaches for calculating inelastic losses, self-energies, and Debye–Waller factors yield significant improvements in amplitude and phase compared to semi-empirical approaches, both for the near edge spectra (XANES) and for EXAFS. We now illustrate these findings with a number of examples; relevant input files for these cases are available from the authors. Some additional applications of FEFF9 can be found in the literature.[79,80]

As a first example, we present results for the XANES (Fig. 4) and the EXAFS (Fig. 5) spectra of Cu. These results clearly show that the MPSE eliminates the spurious effects of the single plasmon-pole approximation and leads to better agreement with experiment.[80] In addition, Fig. 5 shows that our calculation of the many-body amplitude reduction factor S_0^2 is consistent with experiment.

As a second example, we show results for ZnO (Fig. 6) with the MPSE in FEFF9. Again the results show a clear improvement over those in FEFF8 which uses a single plasmon-pole self-energy. Also, as an example of the capabilities of FEFF9

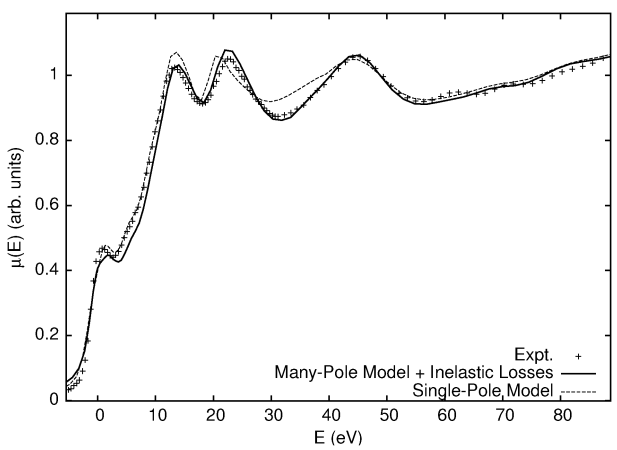

Fig. 4 X-Ray absorption μ *vs.* photon energy E for fcc Cu for our many-pole self-energy model with inelastic losses (solid); the single plasmon-pole model (dashes); and experiment (crosses).[81]

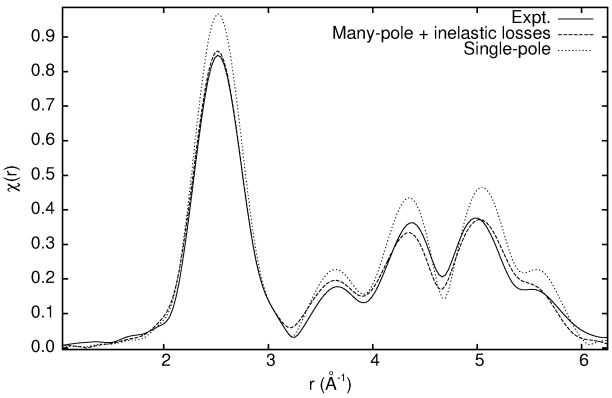

Fig. 5 Fourier transform of the Cu K-edge EXAFS $\tilde{\chi}(r)$ at 10 K *vs.* half MS path-length r with (solid), and without inelastic losses (dots), and from experiment (dashes).[81]

for dichroic spectroscopies, we present results for the X-ray linear dichroism (XLD) of ZnO.

Another interesting result is shown in Fig. 7 for the Mg K-edge XANES of the spinel, $MgAl_2O_4$. Here again, the FEFF9 calculation reproduces the qualitative behavior quite well apart from the position and amplitude of the first peak. This discrepancy is due to either muffin-tin, or finite-cluster size effects, as evidenced by comparing to full potential k-space results such as those of PARATEC.[83]

As an example of the application of FEFF9 to XES we show calculations for NH_4NO_3 from FEFF9 compared to those from the StoBe-deMon code[84,85] in Fig. 8. A detailed analysis of the l-DOS, coupled with auxiliary molecular orbital calculations, allows us to assign all the features in the spectrum. For example, the three peaks observed at 379, 392 and 397 eV are the result of emission from the NO_3^- ion.[85] The intense peak at 392 eV corresponds to emission from the in-plane and out-of-plane π_{NO} bond orbitals, while the less intense peak at 379 eV corresponds to the more bound σ_{NO} orbitals. In the FEFF9 calculations, the splitting of the NO_3^- and

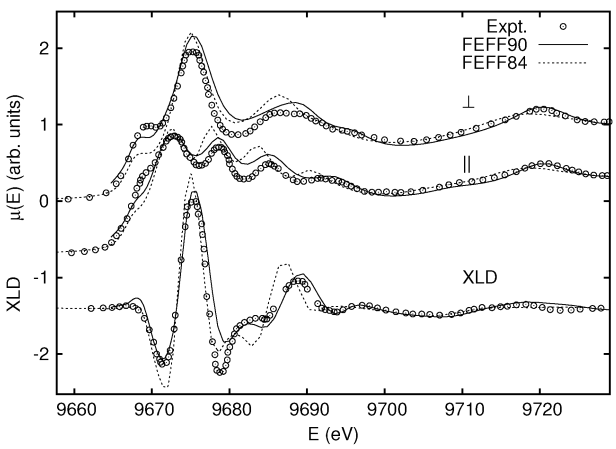

Fig. 6 FEFF9 (solid) calculated results of the Zn K-edge XANES spectra of ZnO compared to those of FEFF8 (dashed) and experimental results (circles).[82] Results are show for polarizations perpendicular (top) and parallel (middle) to the c-axis. Also shown is the X-ray linear dichroism (bottom).

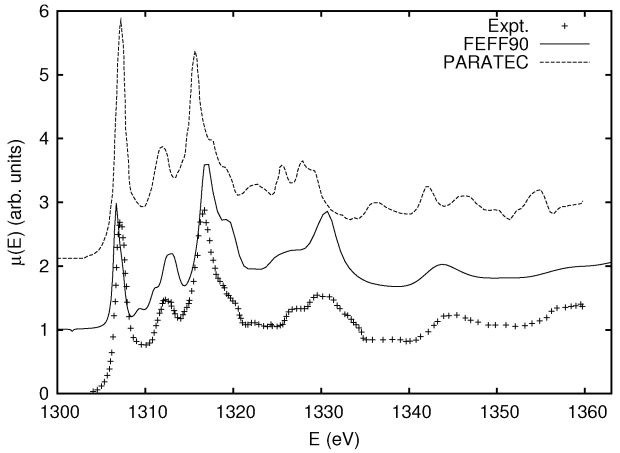

Fig. 7 Mg K-edge XANES of $MgAl_2O_4$ spinel structure. Data[97] (crosses) is compared to calculations from FEFF90 (solid), FEFF84 (dashes), and PARATEC (dots).

NH_4^+ can only be reproduced when a chemical shift of 4.3 eV is included. This shift can now be calculated on-the-fly with FEFF9 and the results are in good agreement with those from StoBe.

As a final example, we present relativistic EELS calculations of the N K-edge of GaN. In Fig. 9 the experimental spectrum[86] is compared to calculations using FEFF9 and the full-potential electronic structure code WIEN2k.[87] We can make two observations. First, the FEFF9 calculation using the new *k*-space approach as outlined in section 3.6, clearly does a better job describing the spectrum than the real-space FEFF9 calculations. This shows that the new formalism avoids finite cluster effects limiting the accuracy of the real-space calculation. Second, the FEFF9 calculation describes experiment better than the WIEN2k calculation. This is especially evident at the onset of the edge, where core hole effects are strong, and where the WIEN2k calculations[12] tend towards the correct edge onset shape as the "supercell" is enlarged. Thus, the FEFF9 *k*-space calculation avoids the pitfalls of either rival approach and yields a result superior to either.

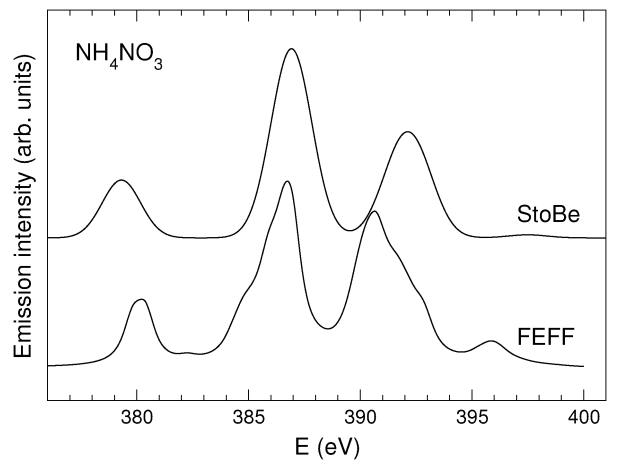

Fig. 8 N–Kα XES spectra of NH_4NO_3 calculated with FEFF[85] and StoBe-deMon[84].

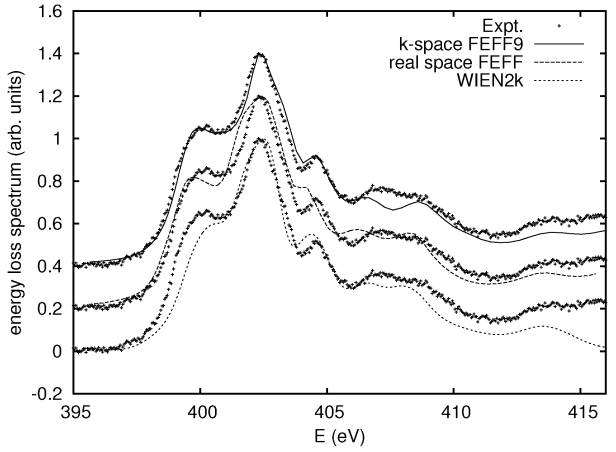

Fig. 9 N K-edge ELNES of GaN at 300 keV beam energy and collection angle 0.3 mrad and convergence angle 0.2 mrad, measured in [100] orientation. Data (crosses; Moreno *et al.*[86]) compared to *k*-space FEFF9 (solid; top), real space FEFF (dashes; middle), and WIEN2K (dots; bottom).

6. Conclusions

In summary, our improved calculations of many-body effects are made possible by three developments: (1) an extension of our RSGF code for full-spectrum calculations; (2) an efficient many-pole representation of the dielectric function; and (3) an efficient Lanczos approach for phonon spectra and DW factors. These developments yield significantly improved treatments of inelastic losses and self-energies due to multi-electron excitations as well as *ab initio* DW factors. All of these many-body effects are important in calculations of optical constants over a broad spectrum, from the UV to X-ray energies.[47] Our approach includes solid state effects (*e.g.*, edge shifts, fine structure, and temperature dependent DW factors) and is applicable to general aperiodic materials. Thus our optical constants complement and can potentially replace empirical tables[88–92] or atomic models[93] for many applications. Finally, the availability of theoretical estimates of various parameters in the theory can lead to improved fits to experiment, and therefore can be useful in many modern EXAFS and XANES analysis techniques.[80,94–96]

We have implemented these developments in the latest version of the FEFF code, FEFF9. In addition, we have extended FEFF9 for calculations of EELS and NRIXS spectra, which were not available in FEFF8. The code also includes JFEFF, a Java-based GUI which enables users to control the input to the code, view plotted results next to experiment, and view 3D renderings of a given system. JFEFF also allows users to control the execution of the FEFF code in a number of environments including single processor, parallel, and even cloud compute environments.[97]

Acknowledgements

We wish to thank A. Ankudinov, D. Bitseff, C. Chantler, X. Gonze, H. Ebert, G. Hug, M. Jaouen, H. Krappe, M. Newville, C. Powell, G. Rivas, H. Rossner, E. Shirley, A. Soininen, C. Hebert, Y. Takimoto and others for helpful

comments, suggestions and contributions. This work is supported in part by the DOE Grant DE-FG03-97ER45623 (JJR, JKK), DE-FG02-04ER1599 (FDV), NIH NCRR BTP Grant RR-01209 (JJK), the F.W.O.-Vlaanderen-Flanders (KJ), and was facilitated by the DOE Computational Materials Science Network.

References

1 G. Onida, L. Reining and A. Rubio, *Rev. Mod. Phys.*, 2002, **74**, 601–659.
2 J. J. Rehr and R. C. Albers, *Rev. Mod. Phys.*, 2000, **72**, 621.
3 J. Vinson, E. L. Shirley, J. J. Rehr and J. J. Kas, unpublished.
4 E. L. Shirley, *Phys. Rev. Lett.*, 1998, **80**, 794–797.
5 J. A. Soininen and E. L. Shirley, *Phys. Rev. B: Condens. Matter Mater. Phys.*, 2001, **64**, 165112.
6 A. L. Ankudinov, Y. Takimoto and J. J. Rehr, *Phys. Rev. B: Condens. Matter Mater. Phys.*, 2005, **71**, 165110.
7 W. von der Linden and P. Horsch, *Phys. Rev. B: Condens. Matter*, 1988, **37**, 8351–8362.
8 E. E. Krasovskii, W. Schattke, V. N. Strocov and R. Claessen, *Phys. Rev. B: Condens. Matter Mater. Phys.*, 2002, **66**, 235403.
9 J. A. Soininen, A. L. Ankudinov and J. J. Rehr, *Phys. Rev. B: Condens. Matter Mater. Phys.*, 2005, **72**, 045136.
10 M. S. Moreno, K. Jorissen and J. J. Rehr, *Micron*, 2007, **38**, 1–11.
11 A. P. Sorini, J. J. Rehr and K. Jorissen, *Electron microscopy and multiscale modeling-emmm-2007*, An International Conference, 2008, pp. 47–52.
12 K. Jorissen, *PhD thesis*, University of Antwerp, 2007.
13 K. Jorissen, J. J. Rehr and J. Verbeeck, *Phys. Rev. B: Condens. Matter Mater. Phys.*, 2010, **81**, 155108.
14 V. P. Sachenko, E. V. Polozhentsev, A. P. Kovtun, Y. F. Migal, R. V. Vedrinski and V. V. Kolesnikov, *Phys. Lett.*, 1974, **48A**, 169–173.
15 P. A. Lee and J. B. Pendry, *Phys. Rev. B: Solid State*, 1975, **11**, 2795–2811.
16 W. L. Schaich, *Phys. Rev. B: Solid State*, 1973, **8**, 4028–4032.
17 C. R. Natoli, D. K. Misemer, S. Doniach and F. W. Kutzler, *Phys. Rev. A: At., Mol., Opt. Phys.*, 1980, **22**, 1104–1108.
18 T. Fujikawa and N. Yiwata, *Surf. Sci.*, 1996, **357–358**, 60–64.
19 A. L. Ankudinov, B. Ravel, J. J. Rehr and S. D. Conradson, *Phys. Rev. B: Condens. Matter Mater. Phys.*, 1998, **58**, 7565.
20 M. P. Prange, J. J. Rehr, G. Rivas, J. J. Kas and J. W. Lawson, *Phys. Rev. B: Condens. Matter Mater. Phys.*, 2009, **80**, 155110.
21 A. P. Sorini, J. J. Kas, J. J. Rehr, M. P. Prange and Z. H. Levine, *Phys. Rev. B: Condens. Matter Mater. Phys.*, 2006, **74**, 165111.
22 J. J. Kas, A. P. Sorini, M. P. Prange, L. W. Campbell, J. A. Soininen and J. J. Rehr, *Phys. Rev. B: Condens. Matter Mater. Phys.*, 2007, **76**, 195116.
23 L. Campbell, L. Hedin, J. J. Rehr and W. Bardyszewski, *Phys. Rev. B: Condens. Matter Mater. Phys.*, 2002, **65**, 064107.
24 J. J. Rehr, M. P. Prange and J. J. Kas, *J. Phys.: Conf. Ser.*, 2009, **190**, 012001.
25 J. J. Rehr, F. Vila, J. P. Gardner, L. Svec and M. Prange, *CiSE*, 2010, **12**(3), 34–43.
26 J. J. Rehr, J. A. Soininen and E. L. Shirley, *Phys. Scr.*, 2005, 207.
27 A. L. Ankudinov, *PhD thesis*, University of Washington, 1996.
28 P. J. Durham, J. B. Pendry and C. H. Hodges, *Comput. Phys. Commun.*, 1982, **25**, 193–205.
29 A. L. Ankudinov, C. E. Bouldin, J. J. Rehr, J. Sims and H. Hung, *Phys. Rev. B: Condens. Matter Mater. Phys.*, 2002, **65**, 104107.
30 H. Ebert, *Rep. Prog. Phys.*, 1996, **59**, 1665–1735.
31 A. Messiah, *Quantum Mechanics*, John Wiley & Sons, Inc., New York, 1962.
32 I. P. Grant, *Adv. Phys.*, 1970, **19**, 747.
33 A. L. Ankudinov, S. I. Zabinsky and J. J. Rehr, *Comput. Phys. Commun.*, 1996, **98**, 359–364.
34 A. L. Ankudinov and J. J. Rehr, *Phys. Scr.*, 2005, 24.
35 L. V. Pourovskii, A. V. Ruban, L. Vitos, H. Ebert, B. Johansson and I. A. Abrikosov, *Phys. Rev. B: Condens. Matter Mater. Phys.*, 2005, **71**, 094415.
36 K. Hatada, K. Hayakawa, M. Benfatto and C. R. Natoli, *Phys. Rev. B: Condens. Matter Mater. Phys.*, 2007, **76**, 060102.
37 M. Taillefumier, D. Cabaret, A. M. Flank and F. Mauri, *Phys. Rev. B: Condens. Matter Mater. Phys.*, 2002, **66**, 195107.
38 Y. Joly, *Phys. Rev. B: Condens. Matter Mater. Phys.*, 2001, **63**, 125120.
39 S. J. Gurman, N. Binsted and I. Ross, *J. Phys. C: Solid State Phys.*, 1986, **19**, 1845–1861.
40 J. J. Rehr and R. C. Albers, *Phys. Rev. B: Condens. Matter*, 1990, **41**, 8139–8149.
41 D. E. Sayers, E. A. Stern and F. W. Lytle, *Phys. Rev. Lett.*, 1971, **27**, 1204–1207.
42 A. Zangwill and P. Soven, *Phys. Rev. A: At., Mol., Opt. Phys.*, 1980, **21**, 1561–1572.
43 L. Hedin and S. Lundqvist, *J. Phys. C: Solid State Phys.*, 1970, **23**, 1.
44 B. I. Lundqvist, *Eur. Phys. J. B*, 1967, **6**, 193.
45 J. A. Soininen, J. J. Rehr and E. L. Shirley, *J. Phys.: Condens. Matter*, 2003, **15**, 2573.
46 I. Campillo, J. Pitarke, A. Rubio, E. Zarate and P. Echenique, *Phys. Rev. Lett.*, 1999, **83**, 2230–2233.
47 M. P. Prange, G. Rivas and J. J. Rehr, *Table of Optical Constants for Mg, Al, Cu, Ag, Au, Bi and C*, http://leonardo.phys.washington.edu/feff/opcons/, 2005.
48 W. S. M. Werner, *Surf. Interface Anal.*, 2001, **31**, 141.
49 J. M. Fernández-Varea, F. Salvat, M. Dingfelder and D. Liljequist, *Nucl. Instrum. Methods Phys. Res., Sect. B*, 2005, **229**, 187–218.
50 F. de Groot and A. Kotani, *Core Level Spectroscopy of Solids*, CRC Press, 2008.
51 P. Kruger and C. R. Natoli, *Phys. Rev. B: Condens. Matter Mater. Phys.*, 2004, **70**, 245120.
52 A. I. Nesvizhskii, A. L. Ankudinov and J. J. Rehr, *Phys. Rev. B: Condens. Matter Mater. Phys.*, 2001, **63**, 094412.
53 F. D. Vila, J. J. Rehr, J. Kas, R. G. Nuzzo and A. I. Frenkel, *Phys. Rev. B: Condens. Matter Mater. Phys.*, 2008, **78**, 121404.
54 E. D. Crozier, J. J. Rehr and R. Ingalls, in *X-ray Absorption: Principles, Applications, Techniques of EXAFS, SEXAFS, and XANES*, Wiley, New York, 1988, p. 375.
55 A. V. Poiarkova and J. J. Rehr, *J. Synchrotron Radiat.*, 1999, **6**, 313–314.
56 A. V. Poiarkova and J. J. Rehr, *Phys. Rev. B: Condens. Matter Mater. Phys.*, 1999, **59**, 948.
57 H. J. Krappe and H. H. Rossner, *Phys. Rev. B: Condens. Matter Mater. Phys.*, 2002, **66**, 184303.
58 E. Sevillano, H. Meuth and J. J. Rehr, *Phys. Rev. B: Condens. Matter*, 1979, **20**, 4908–4911.
59 N. Van Hung and J. J. Rehr, *Phys. Rev. B: Condens. Matter*, 1997, **56**, 43–46.
60 N. Dimakis and G. Bunker, *Phys. Rev. B: Condens. Matter Mater. Phys.*, 1998, **58**, 2467.
61 P. Deuflhard and A. Hohmann, *Numerical Analysis*, de Gruyter, Berlin, 1995.
62 S. Baroni, S. de Gironcoli, A. Dal Corso and P. Giannozzi, *Rev. Mod. Phys.*, 2001, **73**, 515–562.
63 C. Lee and X. Gonze, *Phys. Rev. B: Condens. Matter*, 1995, **51**, 8610–8613.
64 G.-M. Rignanese, J.-P. Michenaud and X. Gonze, *Phys. Rev. B: Condens. Matter*, 1996, **53**, 4488–4497.
65 X. Gonze, J. M. Beuken, R. Caracas, F. Detraux, M. Fuchs, G. M. Rignanese, L. Sindic, M. Verstraete, G. Zerah, F. Jollet, M. Torrent, A. Roy, M. Mikami, P. Ghosez, J. Y. Raty and D. C. Allan, *Comput. Mater. Sci.*, 2002, **25**, 478–492.
66 P. Giannozzi, *et al.*, *Quantum Espresso*, http://quantum-espresso.org/, 2009.
67 M. J. Frisch, G. W. Trucks, H. B. Schlegel, G. E. Scuseria, M. A. Robb, J. R. Cheeseman, J. A. Montgomery, Jr., T. Vreven, K. N. Kudin, J. C. Burant, J. M. Millam, S. S. Iyengar, J. Tomasi, V. Barone, B. Mennucci, M. Cossi, G. Scalmani, N. Rega, G. A. Petersson, H. Nakatsuji, M. Hada, M. Ehara, K. Toyota, R. Fukuda, J. Hasegawa, M. Ishida, T. Nakajima, Y. Honda, O. Kitao, H. Nakai, M. Klene, X. Li, J. E. Knox, H. P. Hratchian, J. B. Cross, C. Adamo, J. Jaramillo, R. Gomperts, R. E. Stratmann, O. Yazyev, A. J. Austin, R. Cammi, C. Pomelli, J. W. Ochterski, P. Y. Ayala, K. Morokuma, G. A. Voth, P. Salvador, J. J. Dannenberg, V. G. Zakrzewski, S. Dapprich, A. D. Daniels, M. C. Strain,

O. Farkas, D. K. Malick, A. D. Rabuck, K. Raghavachari, J. B. Foresman, J. V. Ortiz, Q. Cui, A. G. Baboul, S. Clifford, J. Cioslowski, B. B. Stefanov, G. Liu, A. Liashenko, P. Piskorz, I. Komaromi, R. L. Martin, D. J. Fox, T. Keith, M. A. Al-Laham, C. Y. Peng, A. Nanayakkara, M. Challacombe, P. M. W. Gill, B. Johnson, W. Chen, M. W. Wong and C. Gonzalez, J. A. Pople, *Gaussian 03, Revision B.04*, 2003.
68 P. Fornasini, S. a Beccara, G. Dalba, R. Grisenti, A. Sanson, M. Vaccari and F. Rocca, *Phys. Rev. B: Condens. Matter Mater. Phys.*, 2004, **70**, 174301.
69 G. Dalba, P. Fornasini, R. Grisenti and J. Purans, *Phys. Rev. Lett.*, 1999, **82**, 4240–4243.
70 J. P. Perdew and Y. Wang, *Phys. Rev. B: Condens. Matter*, 1992, **45**, 13244–13249.
71 F. D. Vila, J. J. Rehr, H. H. Rossner and H. J. Krappe, *Phys. Rev. B: Condens. Matter Mater. Phys.*, 2007, **76**, 014301.
72 J. S. Faulkner, *Prog. Mater. Sci.*, 1982, **27**, 1–187.
73 P. Weinberger, *Electron scattering theory for ordered and disordered matter*, Oxford University Press, USA, 1990.
74 A. Gonis and W. H. Butler, *Multiple scattering in solids*, Springer, 1999.
75 A. P. Sorini, J. J. Rehr and Z. H. Levine, *Phys. Rev. B: Condens. Matter Mater. Phys.*, 2008, **77**, 115126.
76 T. T. Fister, F. D. Vila, G. T. Seidler, L. Svec, J. C. Linehan and J. O. Cross, *J. Am. Chem. Soc.*, 2008, **130**, 925.
77 http://aws.amazon.com/.
78 http://aws.amazon.com/ec2/.
79 R. M. van der Veen, J. J. Kas, C. J. Milne, V.-T. Pham, A. E. Nahhas, F. A. Lima, D. A. Vithanage, J. J. Rehr, R. Abela and M. Chergui, *Phys. Chem. Chem. Phys.*, 2010, DOI: 10.1039/b927033g.
80 M. Newville, J. J. Kas and J. J. Rehr, *J. Phys.: Conf. Ser.*, 2009, **190**, 012023.
81 M. Newville, *PhD thesis*, University of Washington, 1995.
82 A. Ney, K. Ollefs, S. Ye, T. Kammermeier, V. Ney, T. C. Kaspar, S. A. Chambers, F. Wilhelm and A. Rogalev, *Phys. Rev. Lett.*, 2008, **100**, 157201.
83 N. Trcera, D. Cabaret, F. Farges, A. M. Flank, P. Lagarde and S. Rossano, *X-ray Absorption Fine Structure-XAFS13: 13th International Conference, AIP Conference Proceedings*, 2007, **882**, 226–228.
84 L. Triguero, L. Pettersson and H. Ågren, *J. Phys. Chem. A*, 1998, **102**, 10599.
85 F. D. Vila, T. Jach, W. T. Elam, J. J. Rehr and J. D. Denlinger, unpublished.
86 M. S. Moreno, S. Lazar, H. W. Zandbergen and R. F. Egerton, *Phys. Rev. B: Condens. Matter Mater. Phys.*, 2006, **73**, 073308.
87 P. Blaha, K. Schwarz, G. Madsen, D. Kvasicka, J. Luitz and K. Schwarz, *TU Wien*, 2001.
88 H. J. Hagemann, W. Gudat and C. Kunz, *J. Opt. Soc. Am.*, 1975, **65**, 742–744.
89 B. L. Henke, E. M. Gullikson and J. C. Davis, *At. Data Nucl. Data Tables*, 1993, **54**, 181–342.
90 *Handbook of Optical Constants of Solids*, ed. E. D. Palik, Academic Press, Orlando, 1985.
91 C. T. Chantler, *J. Phys. Chem. Ref. Data*, 1995, **24**, 71–643.
92 W. T. Elam, B. D. Ravel and J. R. Sieber, *Radiat. Phys. Chem.*, 2002, **63**, 121–128.
93 D. Liberman, J. T. Waber and D. T. Cromer, *Phys. Rev.*, 1965, **137**, A27–A34.
94 H. H. Rossner, D. Schmitz, P. Imperia, H. J. Krappe and J. J. Rehr, *Phys. Rev. B: Condens. Matter Mater. Phys.*, 2006, **74**, 134107.
95 G. Smolentsev and A. V. Soldatov, *Comput. Mater. Sci.*, 2007, **39**, 569–574.
96 M. Benfatto and S. D. Longa, *J. Synchrotron Radiat.*, 2001, **8**, 1087–1094.
97 N. Trcera, D. Cabaret, S. Rossano, F. Farges, A. M. Flank and P. Lagarde, *Phys. Chem. Miner.*, 2009, **36**, 241–257.